Tuning damping and magnetic anisotropy in ultrathin boron-engineered MgO/Co-Fe-B/MgO heterostructures

James Lourembam, Khoong Hong Khoo, Jinjun Qiu, Huiqing Xie, Seng Kai Wong, Qi Jia Yap, Sze Ter Lim*

Dr. J. Lourembam, Dr. J. Qiu, H. Xie, Dr. S. K. Wong, Q. J. Yap, Dr. S. T. Lim
Institute of Materials Research and Engineering, A*STAR (Agency for Science, Technology and Research), 2 Fusionopolis Way, Innovis, #08-03, Singapore 138634
E-mail: jameslourembam.astar@gmail.com

Dr. K.H. Khoo
Institute of High Performance Computing, A*STAR, 1 Fusionopolis Way, #16-16, Connexis North, Singapore 138632

Keywords: Gilbert damping, low-power MRAM, perpendicular magnetic anisotropy

Abstract

Nanometer-thick Co-Fe-B/MgO based structures have been widely accepted as the preferred system for immediate and long-term goals in magnetic random access memory (MRAM) devices because of excellent spin-torque efficiency and promise for high-density MRAM. To realize next-generation ultra-low-power MRAM, further lowering of power consumption in these structures is a crucial ongoing effort. Gilbert damping is one critical material parameter towards lowering energy consumption but is traditionally large (~10^{-2}) in these Co-Fe-B/MgO systems. Here, we report Gilbert damping of $(1.3 \pm 0.3)\times10^{-3}$ from a perpendicular double Co-Fe-B/MgO interface system engineered at different boron compositions. Remarkably, this value is achieved with ~1 nm of Co-Fe-B thickness while maintaining magnetic anisotropy of 0.4 Merg/cc. We also report an unusual damping trend that scales with layer thickness in high-boron content films established from both experiments and first-principles calculations.

1. Introduction

Ultra-low gilbert damping materials based on metallic ferromagnets (FM) are critical requirements towards achieving low-power magnetic random-access memories (MRAM) since current consumption in these devices is directly proportional to the damping constant[1,2]. Damping in metallic FM is typically large because of the presence of conduction electrons which contributes to magnon-elecron scattering[3]. The lowest-reported values of damping in metallic FM (~10^{-3}) are typically found in epitaxially grown thick (>5 nm) samples[4–7]. On the other hand, amorphous Co-Fe-B, the sputtered FM material of choice for MRAM, is not able to reach these damping numbers. In this case, the thickness of Co-Fe-B (t_{CFB}) should be restricted to ~1 nm and grown adjacent to heavy metals with high spin-orbit interaction. These two requirements are essential for achieving perpendicular magnetic anisotropy (PMA), critical for achieving high-density MRAM[1,8,9]. However, these growth requirements lead to unwanted damping enhancement setting a lower-limit of ~10^{-2} in Co-Fe-B-based MRAM structures[10,11].

In the pursuit of low-damping MRAM materials, it was recently discovered that amongst the polycrystalline Co_xFe_{1-x} films the composition $Co_{25}Fe_{75}$ showed the lowest damping ~2×10^{-3} [4,5,12]. This composition has the least magnon-electron scattering[4,12]. Concurrent MRAM stack development saw the emergence of double MgO-based free layer (FL) structures such as MgO/Co-Fe-B/MgO as one of the leading MRAM solutions because of improved performances in spin-torque efficiency and wider operating voltage window[13–20]. Conveniently, damping in these double MgO systems has little contributions from extrinsic effects. This enables damping values of ~5×10^{-3} to be attainable in ~1 nm thick Co-Fe-B[10,21]. Yet, the role of boron composition in damping has largely been overlooked since the extrinsic damping contributions particularly spin-pumping from the adjacent heavy metal, which also serves as a boron sink[10,22,23], largely determines the effective damping. However, with the

double MgO design, this leaves an open question on the impact of boron where spin pumping contributions are minimized[24,25]. Boron engineering is inherently entangled with PMA modification forcing a design predicament between choosing damping optimization and preserving PMA. These questions motivated us to investigate ultra-thin MgO/$(Co_{25}Fe_{75})_{100-x}B_x(t_{CFB})$/MgO structures for perpendicular magnetic tunnel junctions (*p*-MTJs). We found that these structures showed an unprecedented Gilbert damping of (1.3 ± 0.3)×10^{-3} all the while retaining PMA at 360 °C annealing. This is possible by the remarkable discovery of a damping trend that scales directly with film thickness.

2. Results and Discussions

2.1. Boron composition-dependent magnetic anisotropy. We first determine the effective magnetic anisotropy, K_{eff} in our films from the areal difference between out-of-plane (OP) and in-plane (IP) *M-H* measurements[10,26]. The plots of effective magnetic anisotropy per unit area, $K_{eff}t_{CFB}$ as a function of t_{CFB} and annealing temperature (T_A) are shown in **Figure 1**(a), (b), and (c) corresponding to boron compositions (x) at 30 %, 25 %, and 20 % respectively. Our proposed FL structure is shown in Figure 1(d), where the numbers in parenthesis represent nanometers (nm),.

The films with higher boron content at x =25, 30 retain PMA (as indicated by positive values in $K_{eff}t_{CFB}$) for a wide t_{CFB} window extending to ~ 1.2 nm. On the other hand, in x =20 composition films, PMA degrades significantly for $T_A \geq 330$ °C. Within the thickness window of interest for MRAM, the highest effective areal (volume) anisotropies achieved for different boron compositions: x =20, 25, and 30 are —i) ~0.01 erg/cm^2 (0.1 Merg/cc) at 300 °C ii) ~0.06 erg/cm^2 (0.6 Merg/cc) at 330 °C iii) ~0.1 erg/cm^2 (1 Merg/cc) at 380 °C, respectively. For a particular Co-Fe-B composition and thickness, the PMA is maximized at a critical T_A consistent with earlier reports[27,28]. Higher boron content is reported to suppress intermixing[29], which would likely be the reason why the critical T_A is higher in x =30.

Further investigations on the annealing effect on the heterostructure chemistry are discussed in X-ray photoelectron spectroscopy (XPS) section.

As one increases the boron content, the optimum T_A for maximizing K_{eff} also increases. On the other hand, the previous report on boron composition study in Ta/Co-Fe-B/MgO found B =20% to have higher K_{eff} than B =25% even at 350 °C annealing[30]. Clearly, anisotropy trends for double Co-Fe-B/MgO system are different from heterostructures with a boron sink like Ta. To seek insights into the enhancement of K_{eff} for higher boron compositions, we use Density Functional theory (DFT) calculations to obtain layer-resolved magnetic anisotropy (MA). The models MgO (3 ML)/CoFe (5, 7 or 9 ML)/MgO (3 ML) are considered, where ML represent monolayers, and are labeled CF5 and CF7, respectively. Further calculations are also performed on models by introducing B atoms at the CoFe interstitial sites. The models with B dopants are named CFB5 and CFB7 according to the no. of ML. Figure 1(e) and (f) show the models and the corresponding layer-resolved MA comparing CF5 (orange) with CFB5 (green), respectively. Both total and interfacial MA for 5, 7, and 9 ML show enhancement with introduction of B dopant as summarized in **Table 1**. The interfacial MA show at least ~1.7× enhancement with a single boron dopant. To identify whether the PMA enhancement with B-doping is purely due to structural deformities, we also calculated MA for CoFe/MgO interfaces with the elongated c-axis structure taken from the B-doping case but without B. The MA obtained for these strained systems are 0.0 and −0.4 erg/cm^2 for the 5 and 7 CoFe layer systems, respectively, indicating that the enhanced PMA originates from changes in the electronic structure and not geometric distortion induced by B-doping. The interfacial MA originates from the hybridization of ferromagnet *d* and oxygen *p* orbitals[31,32]. We look into interfacial *d*-orbital occupancies by performing partial density-of-states (PDOS) analysis together with perturbation theory to understand the increase in interfacial MA. We find that the interaction between d_{xz} and d_{yz} states mediated by angular momentum operator

L_z gives the dominant contribution to PMA (Supporting Information). Within the framework of Bruno's model[33,34], there is stronger interaction between the unoccupied and occupied d_{xz}/d_{yz} states in B-doping model which is responsible for the enhanced interfacial MA.

Table 1: Total and interfacial MA as determined from DFT.

CoFe ML	No. of B atoms (composition in %)	Total MA in erg/cm^2	MA at CoFe/MgO interface in erg/cm^2
5	0	1.0	2
	1 (16.7%)	3.4	3.5
7	0	0.00	1.28
	1 (12.5%)	2.15	2.22
	2 (22.2 %)	2.79	2.34
9	0	-0.97	1.15
	1 (10%)	2.69	2.10

In reality, annealing is closely interlinked with diffusion and intermixing of elements, which are detrimental to PMA and challenging to model[35–38]. However, given the strong correlations between experimental and theoretical trends, we argue that our proposed models can largely explain the enhancement of PMA in high boron content samples. We note here that if we place boron at the CoFe/MgO interface, calculations show loss of PMA. This case can be ignored for x =25, 30 since our experiments mostly show K_{eff} >0.

2.2. Ultra-low damping. Next, we determine the Gilbert damping, α in these perpendicular FL structures using field-sweep ferromagnetic resonance (FMR) measurements. Here, the microwave frequency (f) and power are kept constant while the applied magnetic field is being swept in the out-of-plane (OP) direction. The analysis for the determination of damping from the FMR spectra is as follows. The FMR absorption peaks of our samples follow a Lorentz absorption and dispersion function and can be well fitted by the equation as[39,40]

$$S_{12} = \frac{A.\Delta H^2}{[(H-H_{res})^2+\Delta H^2)]} + \frac{B.\Delta H(H-H_{res})}{[(H-H_{res})^2+\Delta H^2)]} + \mathrm{C} \qquad (1)$$

where H_{res} is the peak resonance field, ΔH is the full width of half maximum (FWHM), A and B are coefficients, and C represents the spectral background. **Figure 2** (a) shows a representative example of FMR absorption spectra for the x =30 composition annealed at 360 °C. Here, the resonance condition can be fitted by the Kittel equation described as

$$f = \frac{|\gamma|}{2\pi}(H_{res} - 4\pi M_{eff}) \qquad (2)$$

where $|\gamma| = \frac{g_{\perp}\mu_B}{\hbar}$ is the gyromagnetic ratio, $g_{\perp}$ is the spectroscopic splitting factor as determined from fitting the FMR data, μ_B is Bohr magneton, M_{eff} is the effective magnetization. The value of $|\gamma|$ is determined from this Equation and is subsequently used as an input parameter in Equation 3. Then, the damping parameter, α is determined from the equation[41,42]

$$\Delta H = \frac{4\pi\alpha}{|\gamma|} f + \Delta H_0 \qquad (3)$$

where ΔH_0 represents the inhomogeneous linewidth broadening. Figure 2(b) and (c) are plots of the resonance conditions fitted with Equation 2 and linewidth variation fitted with Equation 3, respectively. We choose the OP configuration to minimize two-magnon scattering which is quite significant for ultra-thin films when the FMR is operated in the in-plane configuration[10,43,44]. The general formulation of the experimentally measured linewidth ΔH can be resolved into the following contributions:

$$\Delta H = \Delta H_0 + \Delta H_{gilbert} + \Delta H_{sp} + \Delta H_{TMS} \qquad (4)$$

where the contributions for $\Delta H_{gilbert} = \frac{4\pi\alpha}{|\gamma|} f$ come from gilbert damping, ΔH_{sp} from the spin-pumping, and ΔH_{TMS} from two magnon-scattering. Since MgO is known to suppress spin-pumping[10,24,25] the measured linewidths in our samples, determined from OP FMR (ΔH_{OP}), reduces to $\Delta H_{OP} = \Delta H_0 + \Delta H_{gilbert}$.

Gilbert damping values for MgO (2)/ $(Co_{25}Fe_{75})_{100-x}B_x$ (t_{CFB})/ MgO (2)/ films at selected T_A = 300 °C, 360 °C and 400 °C are shown in top panel of Figure 2 (d), (e) and (f) respectively. Our films show low damping values between $(1.3 \pm 0.3)\times10^{-3}$ [x = 30] and $(9 \pm 1.7)\times10^{-3}$ [x =20]. Such ultra-low damping values are comparable or even lower than those measured in epitaxial Co-Fe or Fe structures[4,5,7,45]. However, Co-Fe-B is preferred over Co-Fe for MRAM because of homogeneity and flatness[46]. Also, our best damping values are lower than previously reported PMA MgO/$Co_{40-x}Fe_xB_{20}$/MgO composition by a factor of 500 %[10]. The best damping values in our stacks are also an order of magnitude lower than the popular Ta/Co-Fe-B/MgO[11,47] MRAM structures and would be amongst the leading choices for ultra-low-power MRAM applications.

Unexpectedly, for boron compositions x =25 and 30, damping increases with t_{CFB}. On the other hand, for x = 20 we do not see an obvious α trend with t_{CFB}. For x =20 films, the available bandwidth is narrower (<13 GHz in OP-FMR), which may lead to larger errors in α. Hence, we would restrict DFT investigation of damping vs thickness trend in just x =25, 30 films.

The inhomogeneous linewidth broadening, which has strong implications in extracting α, is found to be as high as 252 ± 12 Oe in our samples. Bottom panels of Figure 2 (d), (e) and (f) show ΔH_0 plotted against t_{CFB} for samples annealed at 300 °C, 360 °C and 400 °C respectively. We note two important observations— (i) ΔH_0 decreases on increasing t_{CFB} and (ii) x = 30 films, in general, have lower ΔH_0. In PMA systems, ΔH_0 has been strongly correlated with the spatial distribution of magnetic anisotropies which could originate from roughness and interfacial variations[48,49]. Ultrathin thin magnetic layers including Co-Fe-B/MgO systems exhibit large variation in magnetic anisotropies[50,51].

Generally, damping in FL structures is expected to decrease with increasing FM thickness due to spin-pumping effects across the interfaces[4,10,52–54]. Moreover, only a few systems show an increase of damping with FM thickness such as magnetic insulators— $MgAl_{0.5}Fe_{1.5}O_4$, Fe_3O_4,

and $Ni_{0.65}Zn_{0.35}Al_{0.8}Fe_{1.2}O_4$ or >100 nm thick $Ni_{80}Fe_{20}$ films[55–58]. In a previous report, Oogane *et.al.* described that, for 20 nm-thick Co-Fe-B alloys, increasing boron content increases the damping[59]. However, Co-Fe-B films in that report are not annealed and all the boron atoms are expected to remain in the Co-Fe-B layer. A more accurate materials model to explain the thickness trends in damping would be a polycrystalline Co-Fe structure considering boron occupancy, which we will investigate from DFT calculations.

2.3. Thickness-dependent intrinsic damping in high-boron content structures. Our double Co-Fe-B/MgO structures can be considered as systems with minimally varying spin-orbit coupling[4,10]. Under this condition, the intrinsic damping in these systems will be proportional to Fermi level density-of-states i.e. $n(E_F)$[4,10,60–62]. Since spin-pumping is minimal in this system, the experimentally measured damping is expected to be very close to the intrinsic damping.

We model using MgO (3 ML)/CoFe (5, 7,and 9 ML)/MgO (3 ML) slab and consider minimum energy models with 1 B atom and 2 B atom dopants at the CoFe layer consistent with the MA calculations used in Table 1. The CoFe ML are chosen to be consistent with the thickness in FMR measurements i.e. $t_{CFB} \approx$(0.8–1.2) nm. The plot of density-of-states (DOS) around Fermi level (E_F) for our models and the Fermi level DOS values, $n(E_F)$ are shown in **Figure 3**(a) and (b) respectively. We can see from Figure 3(b) that $n(E_F)$ increases with the number of ML of CoFe. This thickness trend agrees well with the FMR experimental observations, for compositions x =25 and 30, where the B atoms residue are expected to remain in the CoFe layer even after annealing. At the same time, this increase does not come directly from B DOS as the individual boron contribution at E_F is only 0.08–0.19 states/eV (about 1 – 2% of the total value) for the systems studied (Supporting Information). We found that the trend remains the same even if the boron were to occupy the interfacial sites. Due to

the discrete nature of DFT modeling, we are not able to keep the B percentage constant but instead, use a fixed number of B dopants for simplicity. However, since DOS generally increases with B doping levels, we expect the DOS increase with CoFe ML will accentuate for a fixed B atomic percentage.

2.4. Elemental spectra at 400 °C. We now turn to look at the chemistry of Co, Fe, and B using X-ray photoelectron spectroscopy (XPS) measurements. To improve the accuracy of the XPS measurements, we prepare thin films with the configuration MgO(5)/$(Co_{25}Fe_{75})_{100-x}B_x$(5)/ MgO(5) annealed at 400 °C. The Co 2*p*, Fe 2*p*, and B 1*s* XPS spectral regions are shown in **Figure 4**(a)-(c) respectively at depths corresponding to the Co-Fe-B layer. Satellite peaks of Co and Fe $2p_{3/2}$ are observed in both x =20 and 30 films and could correspond to CoO $2p_{3/2}$ (~783 eV) and Fe_2O_3 $2p_{3/2}$ (~711 eV)[32,63,64]. The satellite peaks are weaker in x =30 samples. The difference in XPS data is more visible for the B 1*s* spectra, where the peak at ~192 eV corresponds to the boron oxide, BO_x[65] and is much more pronounced in the x = 20 sample [Figure 4(c)]. The peak at ~188 eV corresponds to the B metal peak. The spectra from Co and Fe satellite peaks and B support the argument that higher boron content suppresses intermixing and oxidation. The weakening of PMA for x =20 films is strongly correlated with enhanced boron oxidation as revealed by XPS. It is well-known that annealing can introduce oxidation and diffusion of B [35,36,38,66–69]. The strong evidence of oxidation and elemental diffusion in x =20 films further strengthens the argument for not adopting DFT to model this structure.

3. Conclusion

In summary, we show using broadband FMR and first-principles calculations that decreasing the thickness of MgO/$(Co_{25}Fe_{75})_{100-x}B_x$/MgO films for x =25, 30 reduces the Gilbert damping. This warrants further investigation of device-level spin-torque measurements using these

structures since they are promising alternatives to traditional metallic ferromagnets where damping do not scale with thickness and counteracts the conditions for PMA. Moreover, we also found that boron engineering can enhance PMA by a factor of 5. Surprisingly, first-principles calculations predict 1.7× improvement of interfacial anisotropy with boron engineering. Further optimization would present this heterostructure as an exciting solution for low-power magnetic memory towards applications in internet-of-things and artificial intelligence chips.

4. Experimental Section

Sample Preparation. Double Co-Fe-B/MgO-based FL structures of various ferromagnetic thicknesses (t_{CFB}) are deposited using a Singulus Timaris sputtering system with the following boron compositions: x =30, 25 and 20 in the $(Co_{25}Fe_{75})_{100-x}B_x$ layer, as shown in Figure 1(d). We used 3 different commercially bought targets each corresponding to $(Co_{25}Fe_{75})_{70}B_{30}$, $(Co_{25}Fe_{75})_{75}B_{25}$, and $(Co_{25}Fe_{75})_{80}B_{20}$. We categorize this family of compositions as simply Co-Fe-B. All films are grown under a base pressure of $<4\times10^{-6}$ Pa. Si/SiO_2 wafers are used as substrates and pre-cleaned for 60 s before deposition. MgO and Co-Fe-B are deposited at a power of 4 kW and 0.5 kW, respectively. All samples are annealed under vacuum at select temperatures (300 °C ≤ T_A ≤ 400 °C) for 1 hour in an annealing oven (MVAO, Futek SFM-13-2T-NV) at a ramp rate of < 12 °C/minute and let to cool naturally in vacuum.. During annealing samples are kept under vacuum of pressure < 8×10^{-3} Pa.

Film characterization. Magnetization measurements are performed using Micromag Alternating Gradient Magnetometry (AGM) on samples that are diced to 3×3 mm^2 sized coupons using Okamoto dicer (ADM-6D). The Gilbert damping studies are carried out an home-built vector network analyzer ferromagnetic resonance (VNA FMR) spectroscopy equipped with magnetic fields reaching up to ~6 kOe, and frequencies spanning from 2 to 26 GHz. We use a spring-loaded sample holder to improve the signal-to-noise, the details of

which are described elsewhere[70]. The width of the middle signal line is 117 μm and the gap between the central conductor and the ground planes is 76 μm.

The XPS measurements are conducted ex-situ on a PHI Quantera SXM Scanning X-ray Microprobe with a monochromatic Al *K*α source. The X-ray power is set at 15 kV, 400 W and the measurement spot size is 200 μm. The XPS system is operated on a pass-energy of 55 eV with step size 0.8 eV.

First-principles calculations. DFT calculations using the VASP package with potentials treated using the projector augmented-wave method and virtual crystal approximation (VCA)[71–73]. The CoFe alloy is represented using VCA, where an effective potential obtained by mixing Co and Fe potentials is used to represent the composition of the alloy[73]. A plane-wave energy cutoff of 350 eV is used for all calculations and the exchange-correlation potential is evaluated using the Generalized Gradient Approximation (GGA)[5]. The geometry we construct for our density-of-states calculations is a slab of 5, 7, or 9-atomic layer *bcc* CoFe with 3-atomic layer bulk-like MgO on either side. A vacuum of 10 Å is included along the normal direction to prevent interactions between slabs. The in-plane lattice constants are set to be commensurate with that of bulk MgO which we obtain from our calculations to be a_{CoFe} = 2.97 Å. Structural optimization of our slab is carried out with a force tolerance of 0.01 eV/A and the Brillouin zone is sampled with a Gamma centered 11 x 11 x 1 Monkhorst-Pack grid[74]. For magnetic anisotropy calculations, a higher energy cutoff of 500 eV and denser 29 × 29 × 3 *k*-point grid is employed owing to the higher precision required to resolve the small anisotropy energy differences. In addition, we employ the force theorem and perform non-self-consistent spin-orbit calculations to obtain the total energies for in-plane and out-of-plane magnetizations using a pre-converged charge density obtained from scalar relativistic calculations. The approach has been shown to work well for Co-Fe-B/MgO systems and is significantly more efficient than fully self-consistent spin-orbit calculations[75]. To estimate the atom-resolved MA, we summed up the spin-orbit coupling matrix contributions over all

angular momenta projected on partial waves inside the augmentation sphere centered on each atom[76].

Supporting Information
Supporting Information is available from the Wiley Online Library or from the author.

Acknowledgements
J. Lourembam and K.H. Khoo contributed equally to this work. This work was supported by A*STAR core fund (CF-16), RIE2020 AME Core Fund Grant No. A1818g0042 and SpOT-LITE programme (A*STAR Grant No. A18A6b0057) through RIE2020 funds from Singapore. We also thank Jian Feng Kong and Abhijit Ghosh for scientific discussions. We acknowledge the support of the National Supercomputing Centre (NSCC), Singapore for computational resources.

References

[1] D. Apalkov, B. Dieny, J. Slaughter, *Proc. IEEE* **2016**, *104*, 1796.
[2] Z. Diao, M. Pakala, A. Panchula, Y. Ding, D. Apalkov, L. C. Wang, E. Chen, Y. Huai, *J. Appl. Phys.* **2006**, *99*, 08G510.
[3] Y. Sun, Y.-Y. Song, H. Chang, M. Kabatek, M. Jantz, W. Schneider, M. Wu, H. Schultheiss, A. Hoffmann, *Appl. Phys. Lett.* **2012**, *101*, 152405.
[4] M. A. W. Schoen, D. Thonig, M. L. Schneider, T. J. Silva, H. T. Nembach, O. Eriksson, O. Karis, J. M. Shaw, *Nat. Phys.* **2016**, *12*, 839.
[5] A. J. Lee, J. T. Brangham, Y. Cheng, S. P. White, W. T. Ruane, B. D. Esser, D. W. McComb, P. C. Hammel, F. Yang, *Nat. Commun.* **2017**, *8*, 234.
[6] C. Scheck, L. Cheng, I. Barsukov, Z. Frait, W. E. Bailey, *Phys. Rev. Lett.* **2007**, *98*, 117601.
[7] C. Scheck, L. Cheng, W. E. Bailey, *Appl. Phys. Lett.* **2006**, *88*, 252510.
[8] S. Ikeda, K. Miura, H. Yamamoto, K. Mizunuma, H. D. Gan, M. Endo, S. Kanai, J. Hayakawa, F. Matsukura, H. Ohno, *Nat. Mater.* **2010**, *9*, 721.
[9] D. C. Worledge, G. Hu, D. W. Abraham, J. Z. Sun, P. L. Trouilloud, J. Nowak, S. Brown, M. C. Gaidis, J. O. Sullivan, R. P. Robertazzi, *Appl. Phys. Lett.* **2011**, *98*, 022501.
[10] J. Lourembam, A. Ghosh, M. Zeng, S. K. Wong, Q. J. Yap, S. T. Lim, *Phys. Rev. Appl.* **2018**, *10*, 044057.
[11] T. Devolder, P.-H. Ducrot, J.-P. Adam, I. Barisic, N. Vernier, J.-V. Kim, B. Ockert, D. Ravelosona, *Appl. Phys. Lett.* **2013**, *102*, 022407.
[12] M. A. W. Schoen, J. Lucassen, H. T. Nembach, B. Koopmans, T. J. Silva, C. H. Back, J. M. Shaw, *Phys. Rev. B* **2017**, *95*, 134411.
[13] G. Jan, Y. Wang, T. Moriyama, Y. Lee, M. Lin, T. Zhong, R. Tong, T. Torng, P. Wang, *Appl. Phys. Express* **2012**, *5*, 093008.

[14] H. D. Gan, S. Ikeda, W. Shiga, J. Hayakawa, K. Miura, H. Yamamoto, H. Hasegawa, F. Matsukura, K. Hono, H. Ohno, H. D. Gan, S. Ikeda, W. Shiga, J. Hayakawa, K. Miura, H. Yamamoto, *Appl. Phys. Lett.* **2010**, *96*, 192507.
[15] S. Couet, T. Devolder, J. Swerts, S. Mertens, T. Lin, E. Liu, S. Van Elshocht, G. Sankar Kar, *Appl. Phys. Lett.* **2017**, *111*, 152406.
[16] S. Lee, J. Baek, J. Park, *Sci. Rep.* **2017**, *7*, 11907.
[17] H. Sato, M. Yamanouchi, S. Ikeda, S. Fukami, F. Matsukura, H. Ohno, *Appl. Phys. Lett.* **2012**, *101*, 022414.
[18] H. Kubota, S. Ishibashi, T. Saruya, T. Nozaki, A. Fukushima, K. Yakushiji, K. Ando, *J. Appl. Phys.* **2012**, *111*, 07C723.
[19] J. Lourembam, B. Chen, A. Huang, S. Allauddin, S. Ter Lim, *Appl. Phys. Lett.* **2018**, *113*, 022403.
[20] G. Hu, J. H. Lee, J. J. Nowak, J. Z. Sun, J. Harms, A. Annunziata, S. Brown, W. Chen, Y. H. Kim, G. Lauer, L. Liu, N. Marchack, S. Murthy, E. J. O'Sullivan, J. H. Park, M. Reuter, R. P. Robertazzi, P. L. Trouilloud, Y. Zhu, D. C. Worledge, *Int. Electron Devices Meet. IEDM* **2015**, 668.
[21] S. Srivastava, A. P. Chen, T. Dutta, R. Ramaswamy, J. Son, M. S. M. Saifullah, K. Yamane, K. Lee, K.-L. Teo, Y. P. Feng, H. Yang, *Phys. Rev. Appl.* **2018**, *10*, 024031.
[22] Z. Wang, M. Saito, K. P. McKenna, S. Fukami, H. Sato, S. Ikeda, H. Ohno, Y. Ikuhara, *Nano Lett.* **2016**, *16*, 1530.
[23] X. D. Xu, K. Mukaiyama, S. Kasai, T. Ohkubo, K. Hono, *Acta Mater.* **2018**, *161*, 360.
[24] O. Mosendz, J. E. Pearson, F. Y. Fradin, S. D. Bader, A. Hoffmann, *Appl. Phys. Lett.* **2010**, *96*, 022502.
[25] A. Brataas, Y. Tserkovnyak, G. E. W. Bauer, B. I. Halperin, *Phys. Rev. B* **2002**, *66*, 060404(R).
[26] M. T. Johnson, P. J. H. Blomen, F. J. A. den Broeder, J. J. de Vries, *Rep. Progr. Phys.* **1996**, *59*, 1409.
[27] H. Meng, W. H. Lum, R. Sbiaa, S. Y. H. Lua, H. K. Tan, *J. Appl. Phys.* **2011**, *110*, 033904.
[28] Jaivardhan Sinha, M. Gruber, M. Kodzuka, T. Ohkubo, S. Mitani, K. Hono, M. Hayashi, *J. Appl. Phys.* **2015**, *117*, 043913.
[29] J. P. Pellegren, M. Furuta, V. Sundar, Y. Liu, J. G. Zhu, V. Sokalski, *AIP Adv.* **2017**, *7*, 055901.
[30] S. Ikeda, R. Koizumi, H. Sato, M. Yamanouchi, K. Miura, K. Mizunuma, H. Gan, F. Matsukura, H. Ohno, *IEEE Trans. Magn.* **2012**, *48*, 3829.
[31] S. Kanai, M. Tsujikawa, Y. Miura, M. Shirai, F. Matsukura, H. Ohno, *Appl. Phys. Lett.* **2015**, *105*, 222409.
[32] J. Lourembam, X. Yu, M. P. R. Sabino, R. Sabino, M. Tran, R. W. T. Ang, Q. J. Yap, S. Ter Lim, A. Rusydi, *Phys. Rev. Appl.* **2020**, *14*, 054022.
[33] P. Bruno, *Phys. Rev. B* **1989**, *39*, 865.
[34] M. Zeng, J. Lourembam, S. Ter Lim, *Appl. Phys. Lett.* **2018**, *113*, 192404.
[35] Y. Yang, W. X. Wang, Y. Yao, H. F. Liu, H. Naganuma, T. S. Sakul, X. F. Han, R. C. Yu, *Appl. Phys. Lett.* **2012**, *101*, 012406.
[36] J. C. Read, P. G. Mather, R. A. Buhrman, *Appl. Phys. Lett.* **2007**, *90*, 132503.
[37] D. K. Schreiber, Y. S. Choi, Y. Liu, A. N. Chiaramonti, D. N. Seidman, A. K. Petford-Long, *J. Appl. Phys.* **2011**, *109*, 103909.
[38] Y. Liu, A. N. Chiaramonti, D. K. Schreiber, H. Yang, S. S. P. Parkin, O. G. Heinonen, A. K. Petford-Long, *Phys. Rev. B* **2011**, *83*, 165413.
[39] P. Dürrenfeld, F. Gerhard, J. Chico, R. K. Dumas, M. Ranjbar, A. Bergman, L. Bergqvist, A. Delin, C. Gould, L. W. Molenkamp, J. Akerman, *Phys. Rev. B* **2015**, *92*, 214424.

[40] N. Mecking, Y. . S. Gui, C. M. Hu, *Phys. Rev. B* **2007**, *76*, 224430.
[41] Z. Celinski, B. Heinrich, *J. Appl. Phys.* **1991**, *70*, 5935.
[42] C. Kittel, *Phys. Rev.* **1948**, *73*, 155.
[43] R. Arias, D. L. Mills, *Phys. Rev. B* **1999**, *60*, 7395.
[44] M. J. Hurben, C. E. Patton, *J. Appl. Phys.* **1998**, *83*, 4344.
[45] Y. Li, F. Zeng, S.-L. Zhang, H. Shin, H. Saglam, V. Karakas, O. Ozatay, J. E. Pearson, O. G. Heinonen, Y. Wu, A. Hoffmann, W. Zhang, *Phys. Rev. Lett.* **2019**, *122*, 117203.
[46] D. D. Djayaprawira, K. Tsunekawa, M. Nagai, H. Maehara, S. Yamagata, N. Watanabe, S. Yuasa, Y. Suzuki, K. Ando, *Appl. Phys. Lett.* **2005**, *86*, 092502.
[47] E. C. I. Enobio, H. Sato, S. Fukami, F. Matsukura, *IEEE Magn. Lett.* **2015**, *6*, 5700303.
[48] J. M. Shaw, H. T. Nembach, T. J. Silva, *J. Appl. Phys.* **2010**, *108*, DOI 10.1063/1.3506688.
[49] J. M. Shaw, H. T. Nembach, T. J. Silva, *Phys. Rev. B* **2012**, *85*, 054412.
[50] T. Thomson, G. Hu, B. D. Terris, *Phys. Rev. Lett.* **2006**, *96*, 257204.
[51] Y. Zhang, X. Zhang, N. Vernier, Z. Zhang, G. Agnus, J. R. Coudevylle, X. Lin, Y. Zhang, Y. G. Zhang, W. Zhao, D. Ravelosona, *Phys. Rev. Appl.* **2018**, *9*, 064027.
[52] F. D. Czeschka, L. Dreher, M. S. Brandt, M. Weiler, M. Althammer, I. M. Imort, G. Reiss, A. Thomas, W. Schoch, W. Limmer, H. Huebl, R. Gross, S. T. B. Goennenwein, *Phys. Rev. Lett.* **2011**, *107*, 046601.
[53] Y. Tserkovnyak, A. Brataas, G. E. W. Bauer, *Phys. Rev. Lett.* **2002**, *88*, 117601.
[54] X. Liu, W. Zhang, M. J. Carter, G. Xiao, *J. Appl. Phys.* **2011**, *110*, 033910.
[55] S. Emori, D. Yi, S. Crossley, J. J. Wisser, P. P. Balakrishnan, B. Khodadadi, P. Shafer, C. Klewe, A. T. N'Diaye, B. T. Urwin, K. Mahalingam, B. M. Howe, H. Y. Hwang, E. Arenholz, Y. Suzuki, *Nano Lett.* **2018**, *18*, 4273.
[56] S. Emori, B. A. Gray, H. M. Jeon, J. Peoples, M. Schmitt, K. Mahalingam, M. Hill, M. E. McConney, M. T. Gray, U. S. Alaan, A. C. Bornstein, P. Shafer, A. T. N'Diaye, E. Arenholz, G. Haugstad, K. Y. Meng, F. Yang, D. Li, S. Mahat, D. G. Cahill, P. Dhagat, A. Jander, N. X. Sun, Y. Suzuki, B. M. Howe, *Adv. Mater.* **2017**, *29*, 1701130.
[57] Y. Chen, D. Hung, Y. Yao, S. Lee, H. Ji, C. Yu, *J. Appl. Phys.* **2007**, *101*, 09C104.
[58] S. Serrano-Guisan, H.-C. Wu, C. Boothman, M. Abid, B. S. Chun, I. V. Shvets, H. W. Schumacher, *J. Appl. Phys.* **2011**, *109*, 013907.
[59] M. Oogane, T. Wakitani, S. Yakata, R. Yilgin, Y. Ando, A. Sakuma, T. Miyazaki, *Jpn. J. Appl. Phys.* **2006**, *45*, 3889.
[60] H. Ebert, S. Mankovsky, D. Kodderitzsch, P. J. Kelly, *Phys. Rev. Lett.* **2011**, *107*, 066603.
[61] S. Lounis, M. DosSantosDias, B. Schweflinghaus, *Phys. Rev. B* **2015**, *91*, 104420.
[62] V. Kamberský, *Can. J. Phys* **1970**, *48*, 2906.
[63] A. P. Grosvenor, B. A. Kobe, M. C. Biesinger, N. S. Mcintyre, *Surf. Interface Anal.* **2004**, *36*, 1564.
[64] S. C. Petitto, M. A. Langell, *J. Vac. Sci. Technol. A* **2004**, *22*, 1690.
[65] J. C. Read, P. G. Mather, R. A. Buhrman, *Appl. Phys. Lett.* **2007**, *90*, 132503.
[66] A. K. Rumaiz, C. Jaye, J. C. Woicik, W. Wang, D. A. Fischer, J. Jordan-Sweet, C. L. Chien, *Appl. Phys. Lett.* **2011**, *99*, 222502.
[67] V. Harnchana, A. T. Hindmarch, M. C. Sarahan, C. H. Marrows, A. P. Brown, R. M. D. Brydson, *J. Appl. Phys.* **2013**, *113*, 163502.
[68] A. A. Greer, A. X. Gray, S. Kanai, A. M. Kaiser, S. Ueda, Y. Yamashita, C. Bordel, G. Palsson, N. Maejima, S. H. Yang, G. Conti, K. Kobayashi, S. Ikeda, F. Matsukura, H. Ohno, C. M. Schneider, J. B. Kortright, F. Hellman, C. S. Fadley, *Appl. Phys. Lett.* **2012**, *101*, 202402.
[69] X. Kozina, S. Ouardi, B. Balke, G. Stryganyuk, G. H. Fecher, C. Felser, S. Ikeda, H. Ohno, E. Ikenaga, *Appl. Phys. Lett.* **2010**, *96*, 072105.

[70] S. He, C. Panagopoulos, *Rev. Sci. Instrum.* **2016**, *87*, 043110.
[71] P. E. Blochl, *Phys. Rev. B* **1994**, *50*, 17953.
[72] G. Kresse, J. Furthmiiller, *Comput. Mater. Sci.* **1996**, *6*, 15.
[73] L. Bellaiche, D. Vanderbilt, *Phys. Rev. B* **2000**, *61*, 7877.
[74] Hendrik J. Monkhorst, *Phys. Rev. B* **1976**, *13*, 5188.
[75] K. H. Khoo, G. Wu, M. H. Jhon, M. Tran, F. Ernult, K. Eason, H. J. Choi, C. K. Gan, *Phys. Rev. B* **2013**, *87*, 174403.
[76] S. Steiner, S. Khmelevskyi, M. Marsmann, G. Kresse, *Phys. Rev. B* **2016**, *93*, 224425.

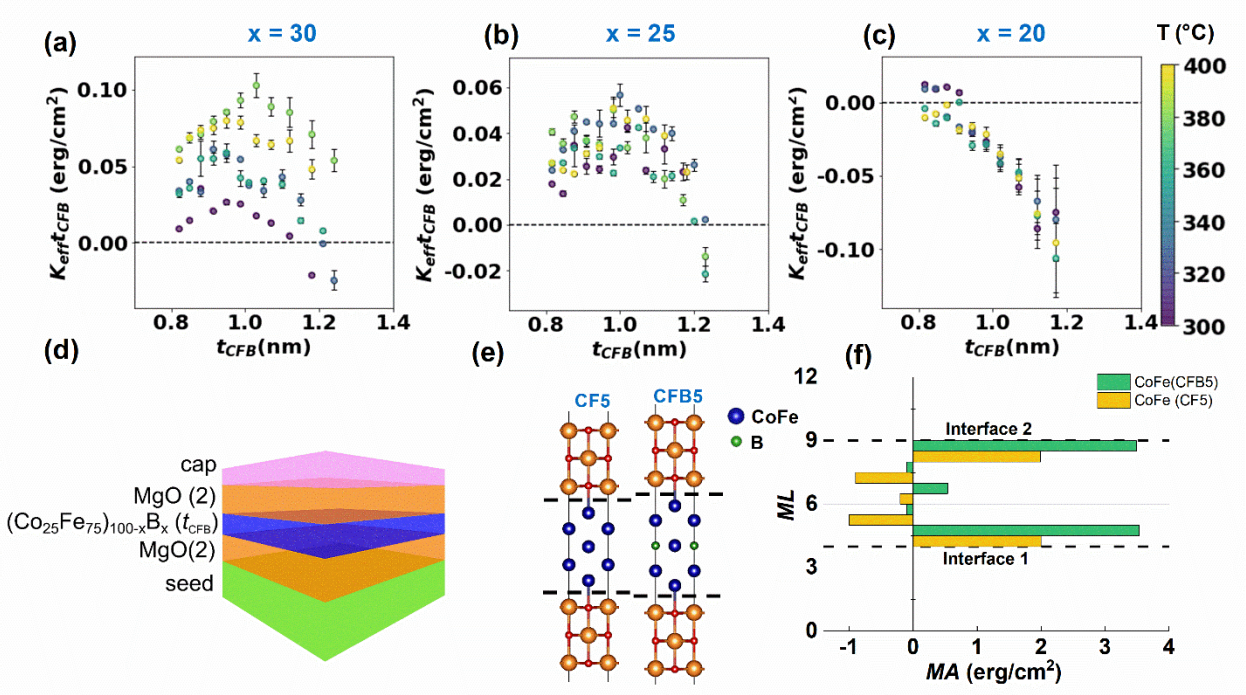

Figure 1: **Boron composition-dependent PMA.** Variation of $K_{eff} \times t_{CFB}$ vs t_{CFB} on double CoFeB/MgO-based FL structures with boron compositions at (a) x =30 (b) x =25 (c) x =20. The different annealing conditions are represented by the color scale. (d) Schematic stack of the sputter-deposited MgO/$(Co_{25}Fe_{75})_{100-x}B_x$/MgO FL structures. (e) Models considering 5 monolayers of CoFe with (CFB5) and without (CF5) boron dopants used in the DFT calculations. (f) Layer-resolved magnetic anisotropies of the CFB5 (green) and CF5 (orange) models. The dashed lines represent interfaces.

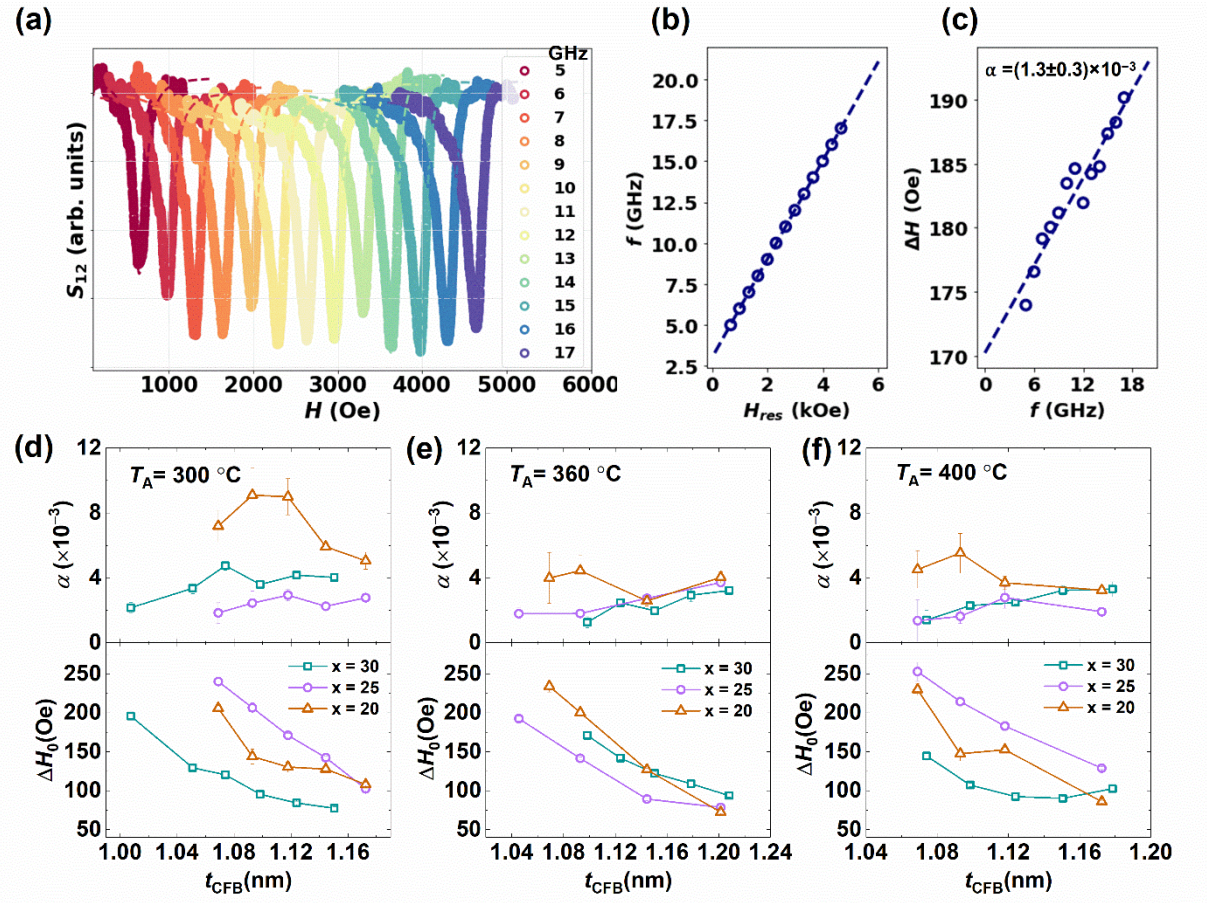

Figure 2: **Boron composition-dependent damping.** (a) OP field-sweep FMR absorption spectra for MgO(2)/$(Co_{25}Fe_{75})_{70}B_{30}$(1.1)/ MgO(2) annealed at 360 °C at various microwave frequencies along with the corresponding Lorentzian fittings. (b) Kittel fitting of the resonance condition and (c) linewidth vs frequency plot to determine damping. Measured α (top panel) and ΔH_0 (bottom panel) as a function of t_{CFB} in MgO/$(Co_{25}Fe_{75})_{100-x}B_x$/MgO structures for various boron compositions at T_A = (d) 300 °C (e) 360 °C and (f) 400 °C.

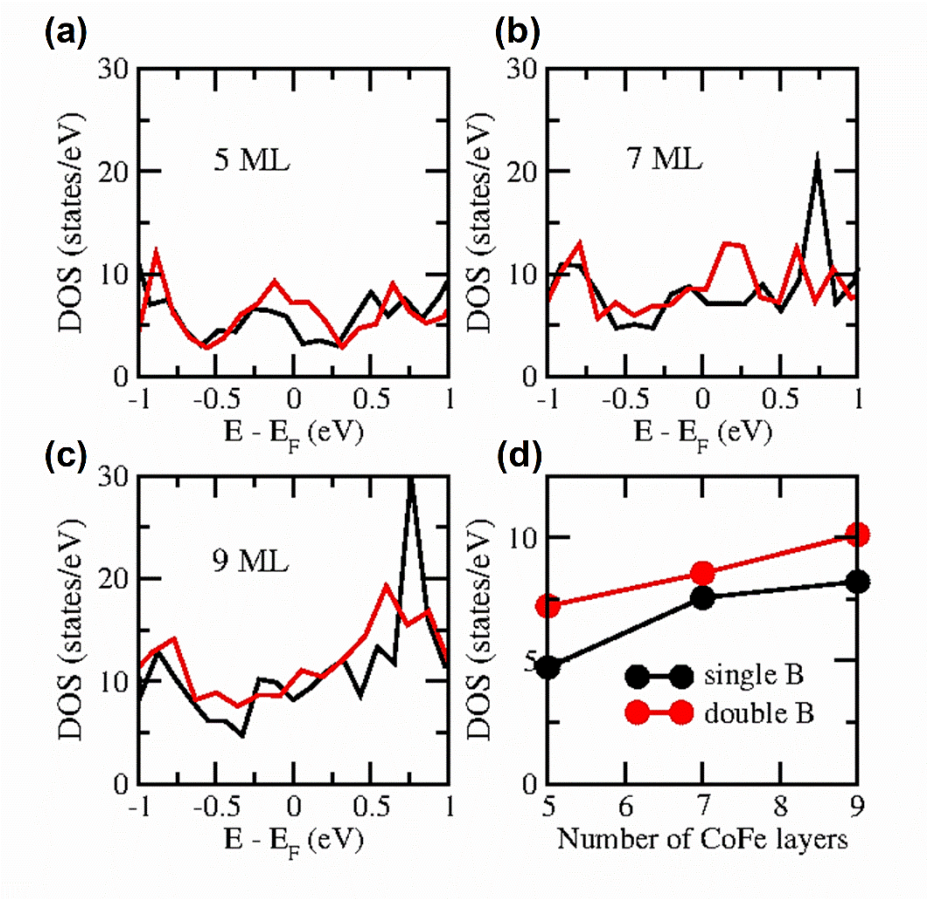

Figure 3: **Thickness-dependent DOS.** (a-c) The density-of-states near the Fermi level for MgO (3ML)/CoFe (5, 7, 9 ML)/MgO (3 ML) models considering various single (black) and double (red) boron occupancies. (d) DOS at E_F versus number of CoFe layers for various B doping levels.

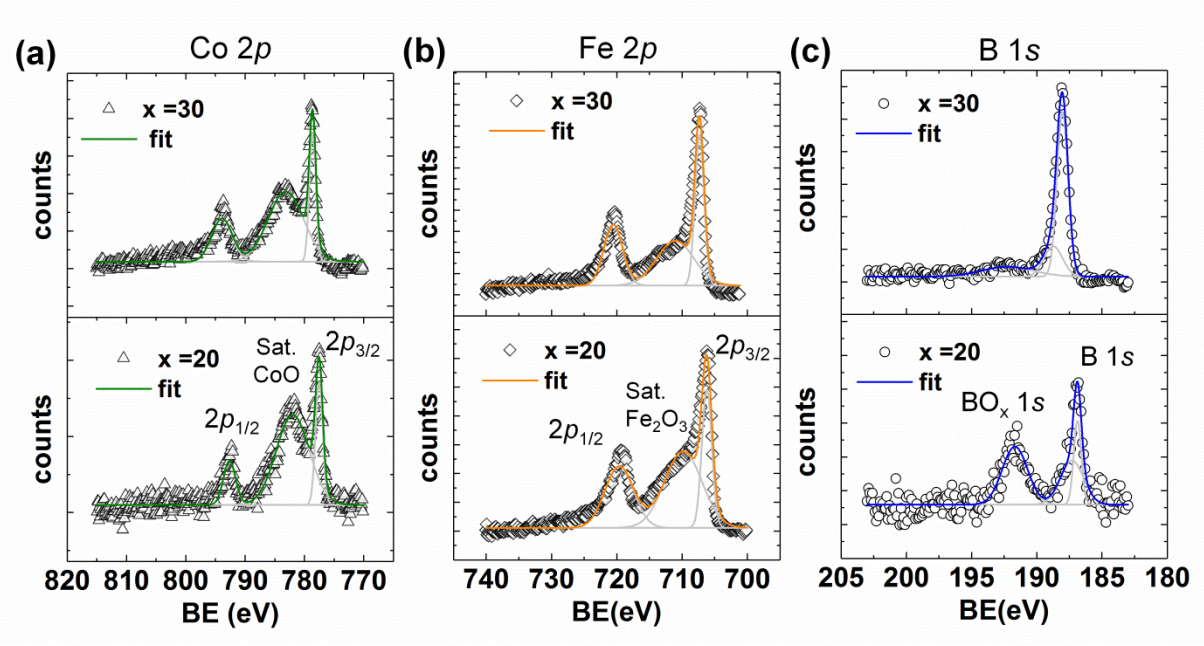

Figure 4: **Elemental spectra at 400 °C.** XPS spectra from (a) Co 2*p* (b) Fe 2*p* and (c) B 1*s* spectral regions for MgO/$(Co_{25}Fe_{75})_{100-x}B_x$/MgO films annealed at 400 °C. The spectral plots in the top and bottom panels correspond to x =30 and x =20 stack structures respectively. The satellite features of Co $2p_{3/2}$ (CoO), Fe $2p_{3/2}$ (Fe_2O_3) as well as BO_x are found to be higher in x =20 samples.

A record low damping of $(1.3 \pm 0.3)\times10^{-3}$ in one-nanometer thick perpendicularly magnetized Co-Fe-B films is achieved. Our work reveals the impact of boron composition on Gilbert damping and magnetic anisotropy. These newly engineered structures will meet the ultra-low power consumption requirements in magnetic non-volatile memories and is viable for immediate technology adoption.

James Lourembam, Khoong Hong Khoo, Jinjun Qiu, Huiqing Xie, Seng Kai Wong, Qi Jia Yap, Sze Ter Lim*

Tuning damping and magnetic anisotropy in ultrathin boron-engineered MgO/Co-Fe-B/MgO heterostructures

ToC figure

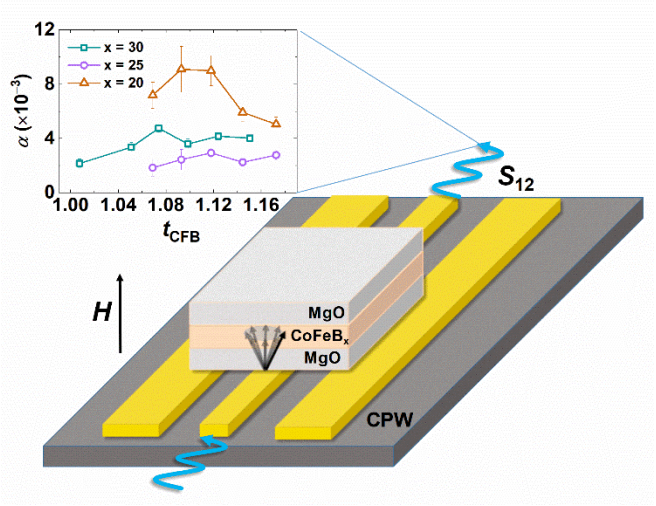

Supporting Information

Tuning damping and magnetic anisotropy in ultrathin boron-engineered MgO/Co-Fe-B/MgO heterostructures

James Lourembam, Khoong Hong Khoo, Jinjun Qiu, Huiqing Xie, Seng Kai Wong, Qi Jia Yap, Sze Ter Lim*

S1. Saturation magnetization

Figure S1 shows saturation magnetization per unit volume of MgO (2)/ $(Co_{25}Fe_{75})_{100-x}B_x$ (t_{CFB})/ MgO films against variation of ferromagnet thickness (t_{CFB}) and boron composition (x). For annealing temperature (T_A) = 300 °C [Figure S1(a)], we find that M_S is distinctively higher for larger x, at any common t_{CFB}. Here, the large values of M_S (> 1500 emu/cc) for x =20 suggest that minimum concentration of boron atoms are left in the ferromagnetic layer. On the other hand, when annealed to 400 °C [Figure S1(b)], the difference in M_S for different x is not as large as a consequence of >30 % reduction of M_S for x = 20 from the values at T_A =300 °C. In Figure S1(c), we show a representative plot for calculating the dead layer thickness which is given by intercept of the linear fit between areal saturation magnetization (M_{sheet}) and t_{CFB}. This is used to determine the dead layer thicknesses (T_d) for various x and T_A. In general, we see a trend of decreasing T_d with increasing T_A. Both x =25, 30 show very small T_d ~0.2 nm when annealed at 380 °C.

The magnetic dead layer can be used to infer the degree of interfacial intermixing. This also provides a context on small deviations between first-principles calculations and experimental results. The magnetic dead layer is a sign of interfacial defects and is associated with lowering interfacial anisotropy[1] and enhancing damping[2].

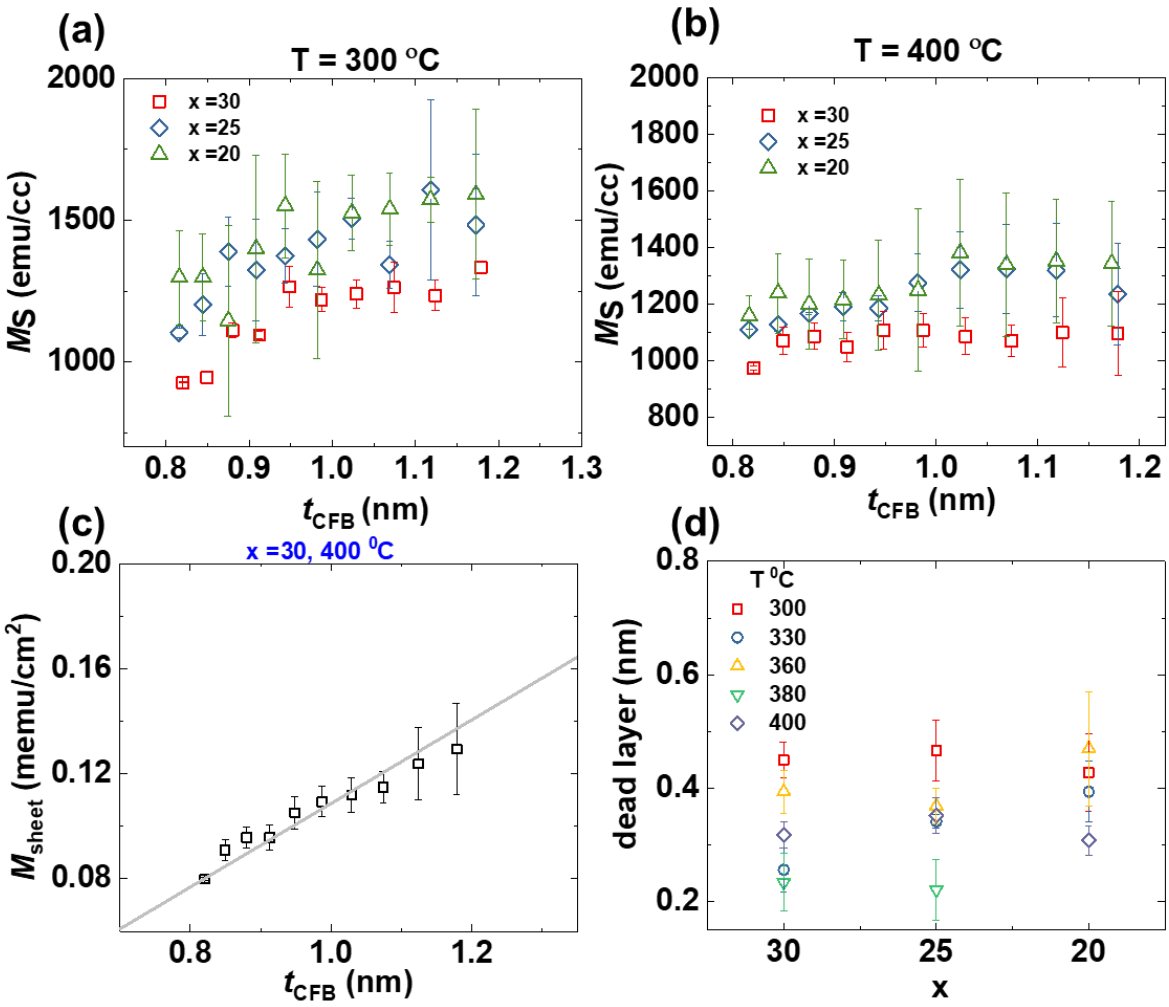

Figure S1: Saturation magnetization (M_S) vs. Co-Fe-B thickness (t_{CFB}) at different boron compositions (x) for annealing temperatures at (a) 300 °C and (b) 400 °C. (c) Plot of the magnetic moment sheet density, M_{sheet} vs t_{CFB} along with a linear fit (gray line). Calculated dead layer thicknesses for various films, which are shown in (d).

S2. Magnetization dynamics

Figure S2(a)-(c) shows dependence of magnetization dynamics parameters— spectroscopic splitting factor ($g_\perp$) and effective magnetization (M_{eff}) on t_{CFB} for x =30, 25 and, 20 respectively. Also shown is the variation of these parameters against T_A. M_{eff} and $g_\perp$ are extracted by fitting the out-of-plane (OP) ferromagnetic resonance spectroscopy results to the resonance condition given by the Kittel equation. We find that $g_\perp$ decreases with increasing

t_{CFB} at all x and T_A variations. The spectroscopic splitting g-factor is directly related to the ratio of the orbital (μ_L) and spin moments (μ_S) through the relation[3]

$$g = 2(1 + \frac{\mu_L}{\mu_S}) \qquad \text{(s1)}$$

The g-factor is known to depend on the chemical composition of FeCo alloys[4]. The out-of-plane g-factor $g_\perp$ is related to the out-of-plane orbital moment ($\mu_L^\perp$) as

$$g_\perp = 2(1 + \frac{\mu_L^\perp}{\mu_S}) \qquad \text{(s2)}$$

$g_\perp$ shown in Figure S2, is higher in x =30 than x =20 films indicating the $\mu_L^\perp$ follows the same variation. This is expected because our first-principles calculations show that interfacial perpendicular magnetic anisotropy is strongly enhanced in high boron content samples. In CoFeB/MgO heterostructures, the interfacial magnetic anisotropy originates from enhanced $\mu_L^\perp$ and has been shown by X-Ray Magnetic Circular Dichroism experiments[5,6].

Moreover, the g-factor is strongly influenced by surface and interface effects as these effects may lead to strong enhancements of $\frac{\mu_L}{\mu_S}$ ratios. The systematic increase in $g_\perp$ with decreasing thickness has been reported before by Shaw et al.[7] in CoFe/Ni multilayers. They found a reciprocal thickness dependence, which they ascribed to the effect of orbital moments originating from the interface. In our systems too, we expect a strong contribution from orbital moments at the interface as shown by the first-principles plot of Fig. 1(f).

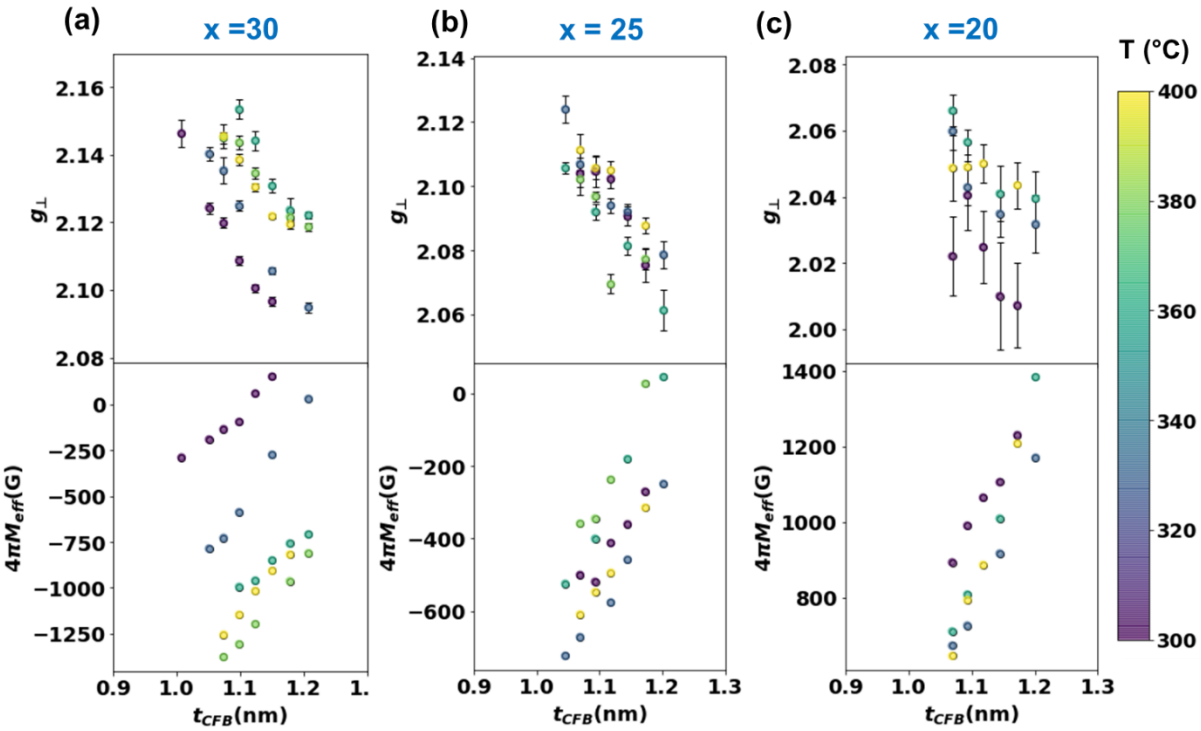

Figure S2: Fitting parameters obtained from ferromagnetic resonance experiments as a function t_{CFB} in MgO/$(Co_{25}Fe_{75})_{100-x}B_x$/MgO structures for boron compositions (a) x =30 (b) x =25 (c) x =20. The top and bottom panels represent $g_\perp$ and $4\pi M_{eff}$ respectively. The various T_A conditions are given by the color scale.

Also, $4\pi M_{eff} = 4\pi M_S - H_K^\perp$, where $H_K^\perp$ is the perpendicular anisotropy saturation field, becomes more negative with reducing thickness giving an independent verification for the presence of interfacial anisotropy. M_{eff} for x =30, 25 show negative values indicating the presence of perpendicular magnetic anisotropy (PMA) whereas, for x =20, the values are positive due to degradation of PMA.

Figure S3 shows comparisons of FMR linewidths taken in OP (blue symbols) and in-plane, IP (green symbols) configuration for various MgO/$(Co_{25}Fe_{75})_{100-x}B_x$/MgO films. Regardless of the composition x value and annealing temperature, we observe strong enhancement of ΔH in IP FMR measurements, which is about twice as large as those from OP FMR. The dashed

lines represent the linear fittings, the slope of which can be used to extract damping. Generally, the slopes of IP FMR measurements are higher at T_A = 360 °C showing a much stronger difference with the OP FMR slopes. These results indicate the presence of strong two-magnon scattering in our systems which is expected to be largest in the IP FMR measurement[8–10].

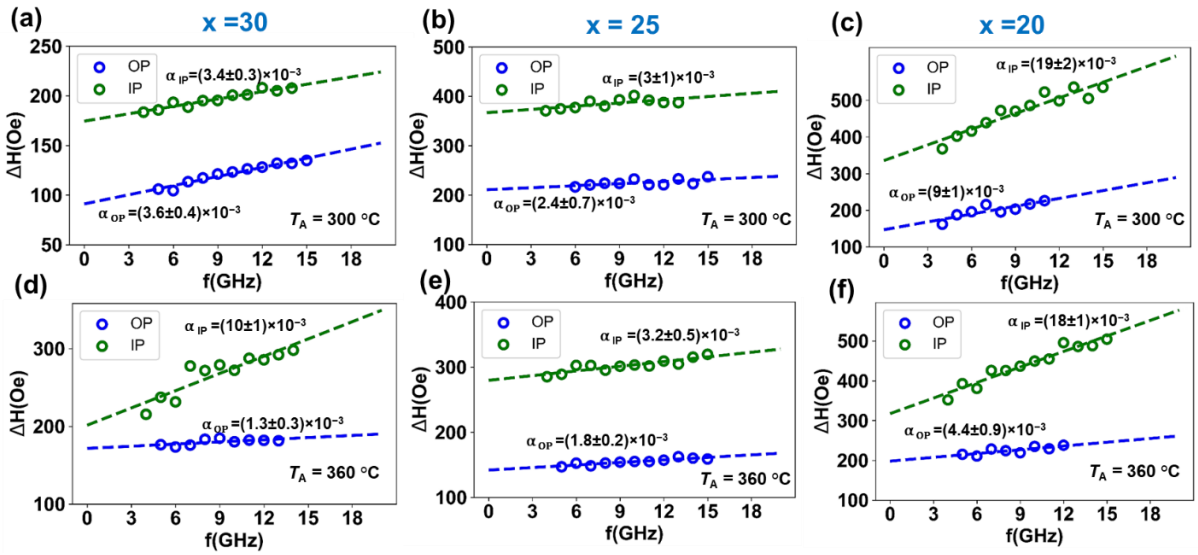

Figure S3: Comparison of linewidth vs resonance frequencies from OP (blue) and IP (green) FMR measurements along with linear fittings, which are used to determine damping. (a)-(c) represents linewidths for MgO/$(Co_{25}Fe_{75})_{100-x}B_x$/MgO films annealed at 300 °C while those in (d)-(f) are annealed at 360 °C. The thickness of the ferromagnets are ~1.1 nm. The damping values for both OP (α_{OP}) and IP (α_{OP}) measurements are also labelled.

Since the strongest anisotropy (1 Merg/cc) is found in x =30 samples when annealed under 380 °C, we also proceeded to determine the damping for the set of samples with T_A = 380 °C. However, the lowest damping value is found to be (2.1 ± 0.3)×10^{-3} for this set of films as shown in Figure S4(a). The corresponding linewidth broadening parameter is shown in Figure S4(b).

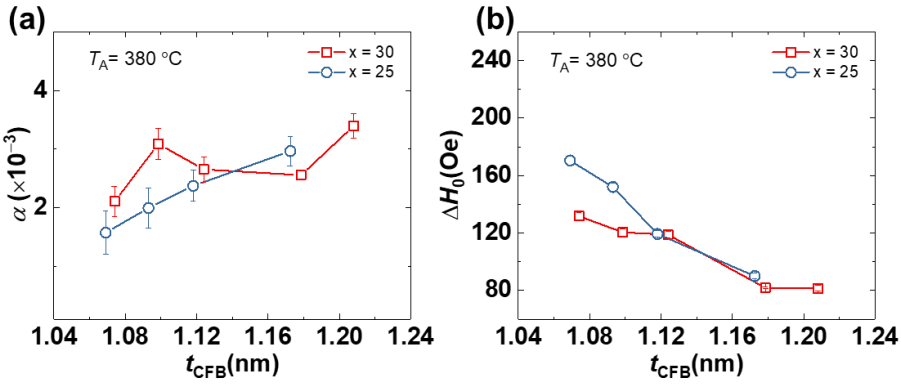

Figure S4: (a) α and (b) ΔH_0 as a function of t_{CFB} in MgO/$(Co_{25}Fe_{75})_{100-x}B_x$/MgO films as determined from FMR measurements at T_A = 360 °C.

S3. Calculation of density-of-states

To understand the energetics of B doping, we employ the MgO(3 ML)/CoFe(7, 9 ML)/MgO(3 ML) models and start introducing B at different sites as shown in Figure S5 (a) and (b) for 7 and 9 ML CoFe heterostructures respectively. For each of these systems, we compute the defect formation energy (E_{form}), defined as $(E_{CoFeB} - E_{CoFe} - n_B \times E_{bulk\_B})/n_B$ and these are plotted in Figure S5(c) for various single and double boron occupancy scenarios. Here, E_{CoFeB} and E_{CoFe} are the total energies of the B-doped and bare CoFe models respectively, n_B is the number of dopant B atoms, and E_{bulk_B} is the energy per B atom in bulk boron. The models 1A and 2A are found to have the lowest E_{form} for a single B dopant. The two B configurations 1E and 2F are based on the lowest energy single B models 1A and 2A but with B dopants repeated on both CoFe/MgO interfaces.

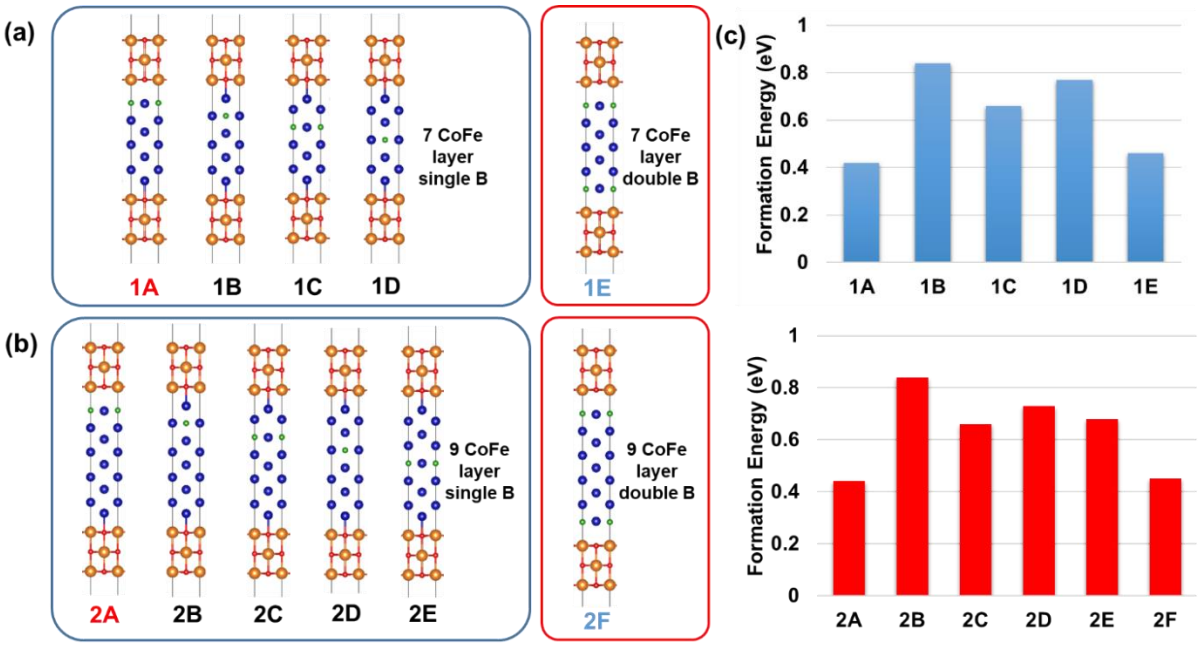

Figure S5: Schematic atomic representation of the various models considered for first-principles calculations. (a) The models from 1A–1E consider boron atoms interstitially located in various positions of the MgO (3 ML)/CoFe (7 ML)/MgO (3 ML) heterostructure (b) the models 2A–2F consider boron atoms in MgO (3 ML)/CoFe (9 ML)/MgO (3 ML) heterostructure. The corresponding formation energies due to the introduction of boron defects are shown in (c).

We perform a partial density-of-states (PDOS) analysis together with perturbation theory on two structures— MgO (3 ML)/CoFe (7 ML)/MgO (3 ML) and MgO (3 ML)/CoFe (7 ML, double B doping)/MgO (3 ML). As seen in the atom-resolved magnetic anisotropy (MA) of Fig. 1(d), perpendicular MA mostly originates from the CoFe atom at the MgO interface, thus we will focus on this atom. The *d*-orbital PDOS on the interface CoFe is plotted in Figure S6.

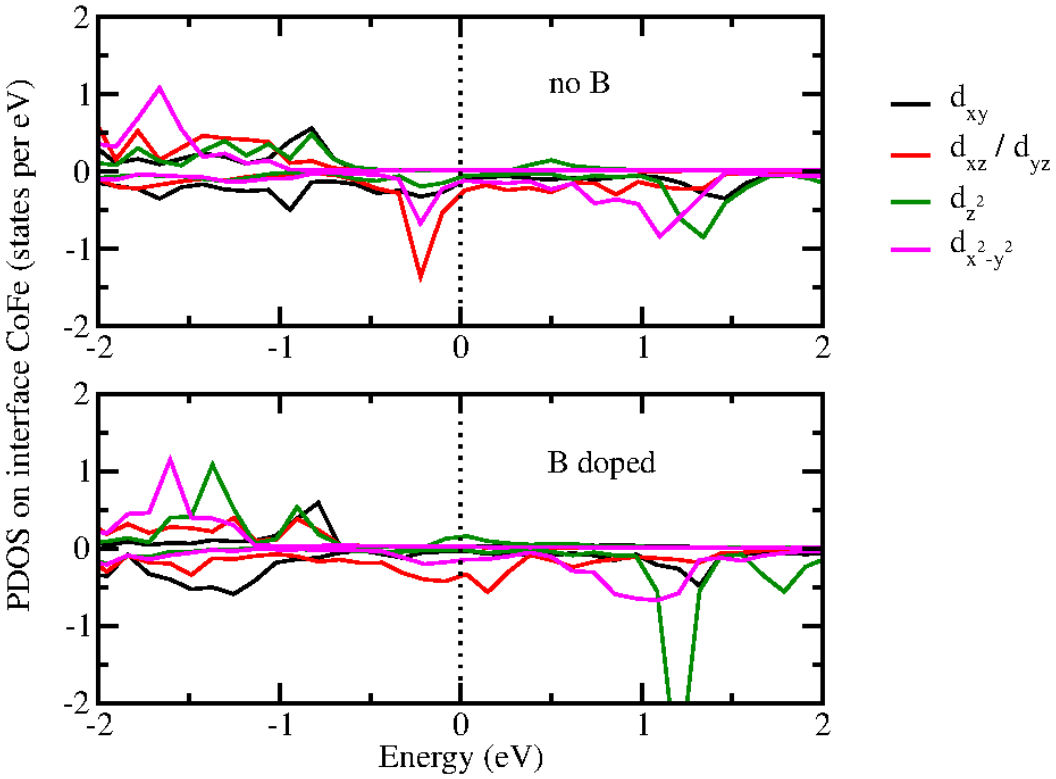

Figure S6: PDOS of *d*-orbitals on CoFe atom at MgO interface. Top and bottom panels are for structures without and with B doping respectively.

We see that the PDOS is mostly the minority spin about the Fermi level (negative PDOS at 0 eV), thus we only need to consider the interaction between occupied and unoccupied states of the same spin to a first approximation. Under this assumption, the MA can be expressed as[11]

$$MA = \xi \sum_{o,u} \frac{|\langle\psi_o|L_z|\psi_u\rangle|^2 - |\langle\psi_o|L_x|\psi_u\rangle|^2}{E_o - E_u} \qquad \text{(s3)}$$

where ξ is the spin-orbit coupling strength; ψ_o (ψ_u) represent the occupied (unoccupied) minority-spin states with an energy of E_o (E_u); and L_z and L_x are the orbital angular momentum operators. Also, it is known that L_z couples orbitals d_{xz} to d_{yz} and d_{xy} to $d_{x^2-y^2}$, while L_x couples d_{yz} to d_{z^2}, d_{yz} to $d_{x^2-y^2}$ and d_{xz} to d_{xy}. Combining this with information from the PDOS plots, we see that interaction between d_{xz} and d_{yz} states mediated by L_z gives the dominant contribution to perpendicular MA about E_F. With this reasoning, it is easy to see why MA is larger for the B-doped case as there is a d_{xz}, d_{yz} peak straddling the Fermi level

leading to maximum interaction between occupied and unoccupied states, while the undoped case has most of this peak located on the occupied side leading to reduced PMA. The interfacial MA for 7 ML and 9 ML systems are very similar but is larger for 5 ML systems is due to quantum confinement. The atom-resolved MA is qualitatively very similar between those obtained using VCA vs actual Co/Fe atoms. The use of VCA gives the advantage of not having to make arbitrary choices about the placement of Co and Fe, making VCA results more general and unbiased.

Figure S7 shows the atom-resolved DOS in MgO (3ML)/CoFe (9ML) /MgO (3 ML) by considering different boron occupancy models in the CoFe layer — single boron, two boron. The models are consistent with Figure 4 DOS and follows 2C occupancy model for single B case and for double B case, the B atoms are occupy the similar sites as 2C and 2E. CoFe has a much higher DOS at the Fermi level than B. The boron atom has a strong effect on the surrounding atoms, both structurally and electronically, thus even though the boron DOS is small, the total DOS is significantly modified.

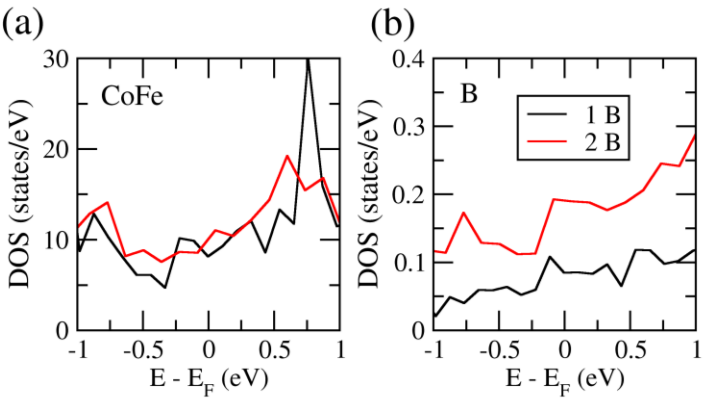

Figure S7: Atom-resolved density-of-states plots for MgO(3ML)/CoFe(9ML)/MgO(3ML) with 2C occupancy model for single B case and B positions corresponding to 2C and 2E models for double B case.

S4. X-ray photoelectron spectroscopy

Figure S8(a)-(c) shows the Co 2*p*, Fe 2*p* and B 1*s* XPS spectral regions of the double Co-Fe-B/MgO films annealed at 300 °C respectively. Unlike the 400 °C, we do not see significant difference between the x =20 and 30 films. The satellite peak in Co 2*p* XPS spectra is slightly diminished in x =20 as compared to x =30 structure. Also, the BO_x 1*s* peak is evidently weak in both x =20 and 30 films.

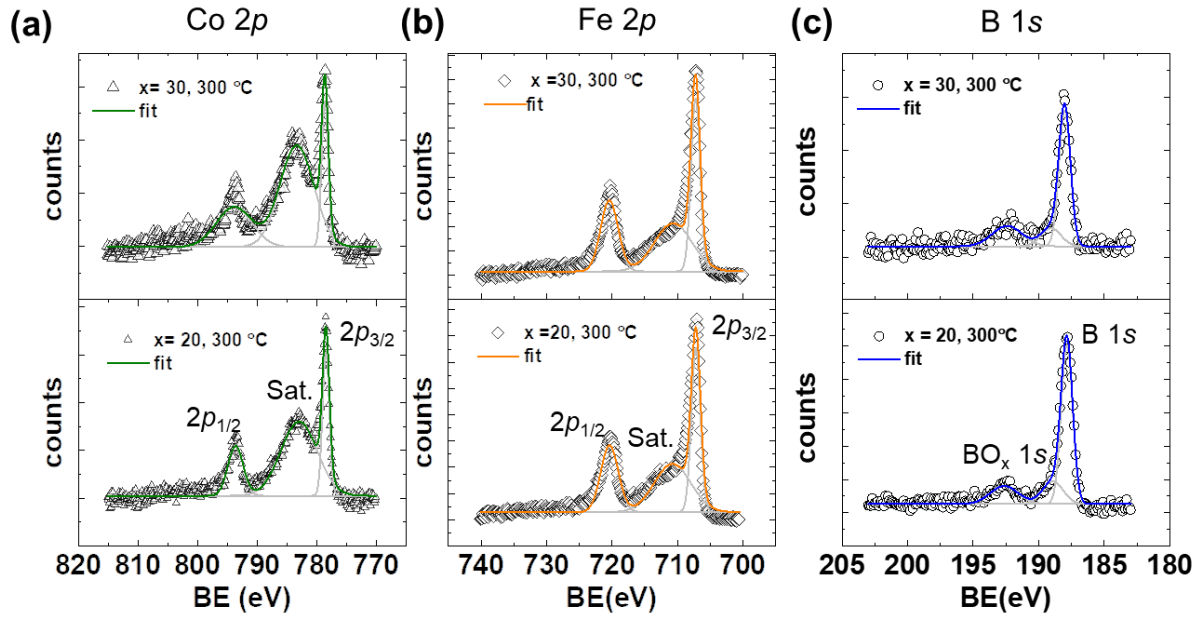

Figure S8. XPS spectra of MgO/$(Co_{25}Fe_{75})_{100-x}B_x$/MgO films annealed at 300 °C corresponding to (a) Co 2*p* (b) Fe 2*p* and (c) B 1*s* spectral regions. Top and bottom panels represent x =30 and x =20 stack structures respectively.

The depth-resolved XPS profiles of relevant elements in our free layer films annealed at 400 °C are shown in Figure S9(a). XPS depth profiling is achieved using Ar^+ ion etching, and the ion raster scanned over 2 × 2 mm area on the sample. The ion energy of the Ar^+ sputter gun is set at 1 kV and the ion beam current to 1 μA. Atomic percentages are extracted from the Multipak software after applying a Shirley baseline to detailed scans around each set of peaks.

The atomic percentage profiles are as expected. By looking at the boron profiles across different compositions and T_A [Figure S8(b) bottom panel], for the same x, we do not find noticeable variation of atomic percentages with T_A, which is likely due to the choice of thick Co-Fe-B (5 nm). The Co atomic percentage remains similar across various samples as shown in the top panel of Figure S9(b). However, Co and B peak positions have shifted deeper for x =20 at T_A = 400 °C. Previous reports have also reported large amounts of boron diffusion in $Co_{40-x}Fe_xB_{20}$ when annealed at temperatures ≥350 °C[12–14].

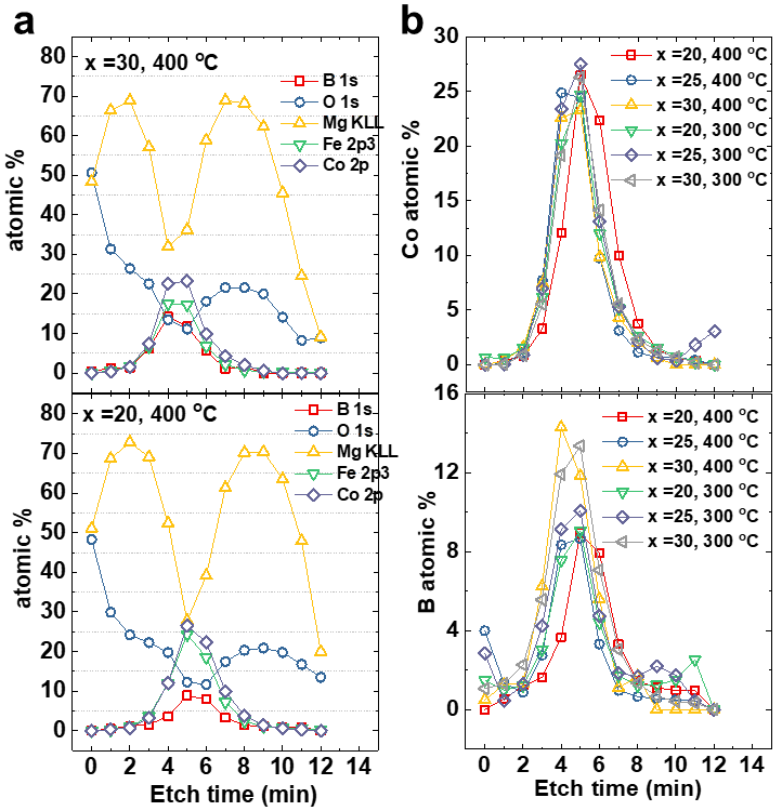

Figure S9. (a) XPS elemental resolved depth profile of x =30 (top panel) and x =20 (bottom panel) films annealed at 400 °C. (b) XPS depth profile of various samples comparing Co (top) and B (bottom) atomic percentages.

S5. Cross-section transmission electron microscopy

Cross-sectional film microstructures are characterized using Tecnai G2 F20 transmission electron microscopy (TEM) with electron beam operated at 200 kV. Sample preparation for

TEM is done using a focused 30 kV Ga+ ion beam followed by 5 kV final cleaning (model FEI DA300). Figure S10 shows cross-section (TEM) data for (a) as-desposited and (b) 400 °C annealed MgO(2)/$(Co_{25}Fe_{75})_{70}B_{30}$(1.5)/MgO(2) films. Also shown are the nano diffraction pattern indicating that the MgO layer is crystallized in both films. However, the Co-Fe-B layer is completely amorphous in as-deposited sample while the annealed sample shows local crystallization. The diffraction spots and the halo rings are not discernable in an amorphous layer.

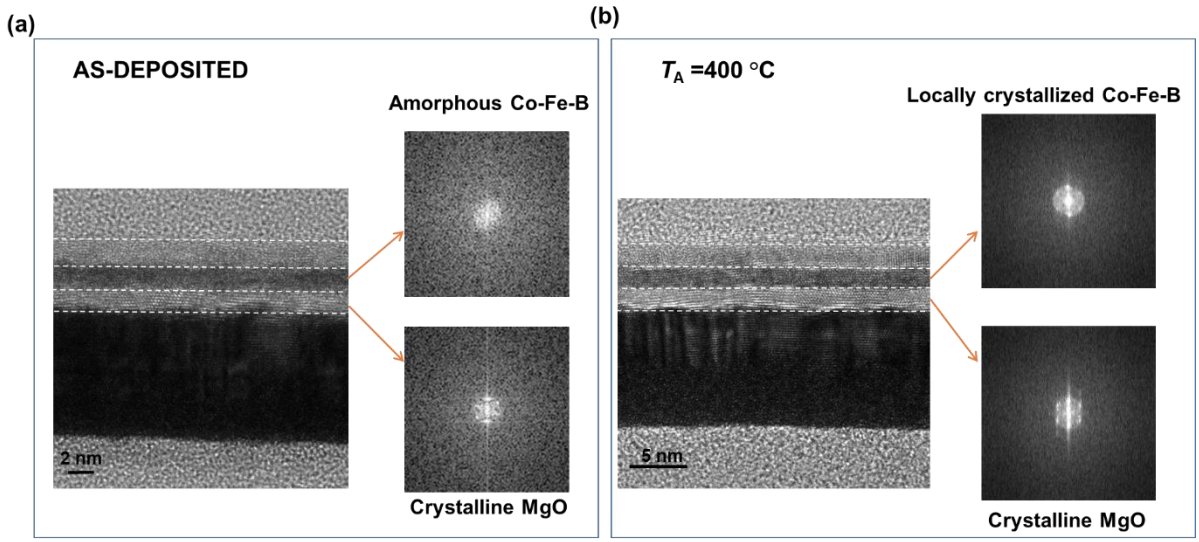

Fig S10: Comparison of cross-section TEM images of (a) as-depsoited and (b) 400 °C annealed MgO(2)/$(Co_{25}Fe_{75})_{70}B_{30}$(1.5)/MgO(2) films. Also shown in the top and bottom panels are fast-fourier transform (FFT) showing diffraction patterns of regions in the CoFeB and MgO layers, respectively.

S6. Micromagnetic simulations

We performed micromagnetic simulations using the MuMax3[15] software on a defined cylinder of diameter 50 nm and thickness 1 nm to determine spin torque switching currents. The magnetic parameters used in the simulation are: exchange constant $A = 14 \times 10^{-12}\, J/m$, saturation magnetization $M_s = 1250 \times 10^3\, A/m$, uniaxial anisotropy $K_u = 1.1 \times 10^6\, J/m^3$ and α =0.0013 as determined from magnetometry and FMR. A 20 ns pulse current is sent to

the structure at different current amplitudes. For 20 ns pulse, the switching current threshold is found to be 2×10^{10} A/m^2.

Further, these simulated values are compared against actual device measurements for a MgO/$Co_{20}Fe_{60}B_{20}$/MgO structure as shown in Table S1. We see that our high boron content samples have superior performance in switching current (80% reduction) but not in thermal stability, Δ (~16% reduction). The thermal stability is calculated from the equation[16]

$$\Delta = \frac{K_{eff} t_{CFB} \pi D^2}{4 k_B T} \quad \text{(s4)}$$

where $K_{eff}t_{CFB}$ is the magnetic anisotropy per unit area, D is the diameter of the nanomagnet, k_B is Boltzmann constant and T is the operation temperature.

Free layer structure	Approach	Switching current	Thermal stability
MgO/$Co_{20}Fe_{60}B_{20}$/MgO	Device characterization[17]	1×10^{11} A/m^2 (20 ns)	56 k_BT
MgO/$(Co_{25}Fe_{75})_{70}B_{30}$/MgO	Film characterization+simulations [This work]	2×10^{10} A/m^2 (20 ns)	47 k_BT

Table S1: Comparison of switching current and thermal stability with device literature work.

References

[1] S. Shen, D. Lee, C. Cheng, W. Chan, G. Chern, *IEEE Trans. Magn.* **2019**, *55*, 3400205.
[2] N. Sato, K. P. O'Brien, K. Millard, B. Doyle, K. Oguz, *J. Appl. Phys.* **2016**, *119*, DOI 10.1063/1.4941943.
[3] C. Kittel, *Phys. Rev* **1949**, *76*, 743.
[4] F. Schreiber, J. Pflaum, Z. Frait, T. Mühge, J. Pelzl, *Solid State Commun.* **1995**, *93*, 965.
[5] J. Lourembam, X. Yu, M. P. R. Sabino, R. Sabino, M. Tran, R. W. T. Ang, Q. J. Yap, S. Ter Lim, A. Rusydi, *Phys. Rev. Appl.* **2020**, *14*, 054022.
[6] S. Kanai, M. Tsujikawa, Y. Miura, M. Shirai, F. Matsukura, H. Ohno, *Appl. Phys. Lett.* **2015**, *105*, 222409.
[7] J. M. Shaw, H. T. Nembach, T. J. Silva, *Phys. Rev. B* **2013**, *87*, 054416.
[8] X. Liu, W. Zhang, M. J. Carter, G. Xiao, *J. Appl. Phys.* **2011**, *110*, 033910.
[9] M. J. Hurben, C. E. Patton, *J. Appl. Phys.* **1998**, *83*, 4344.
[10] R. Arias, D. L. Mills, *Phys. Rev. B* **1999**, *60*, 7395.
[11] P. Bruno, *Phys. Rev. B* **1989**, *39*, 865.
[12] A. K. Rumaiz, C. Jaye, J. C. Woicik, W. Wang, D. A. Fischer, J. Jordan-Sweet, C. L. Chien, *Appl. Phys. Lett.* **2011**, *99*, 222502.
[13] Y. Lu, B. Lépine, G. Jézéquel, S. Ababou, M. Alnot, J. Lambert, A. Renard, M. Mullet, C. Deranlot, H. Jaffrès, F. Petroff, J. M. George, *J. Appl. Phys.* **2010**, *108*, 043703.
[14] V. Harnchana, A. T. Hindmarch, M. C. Sarahan, C. H. Marrows, A. P. Brown, R. M. D.

Brydson, *J. Appl. Phys.* **2013**, *113*, 163502.
[15] A. Vansteenkiste, J. Leliaert, M. Dvornik, M. Helsen, F. Garcia-sanchez, B. Van Waeyenberge, *AIP Adv.* **2018**, *4*, 107133.
[16] D. Apalkov, B. Dieny, J. Slaughter, *Proc. IEEE* **2016**, *104*, 1796.
[17] J. Lourembam, B. Chen, A. Huang, S. Allauddin, S. Ter Lim, *Appl. Phys. Lett.* **2018**, *113*, 022403.